

Current Imbalance in Parallel Battery Strings Measured Using a Hall-Effect Sensor Array

Robert Luca, Michael Whiteley, Toby Neville, Tom Tranter, Julia Weaving, James Marco, Paul R. Shearing, and Dan J. L. Brett*

Herein, individual cell currents in parallel connected battery strings are measured using micro-Hall-effect sensors. Cells are routinely connected in electrical series and parallel to meet the power and energy requirements of automotive and consumer electronics applications. Cells connected in series have been extensively studied; however, cells in parallel are often assumed to be a “black box” in battery management systems. Poor pack design can result in positive feedback between current and temperature differentials along the parallel string, driving greater levels of heterogeneous behavior and uneven degradation. Herein, a noninvasive multisensor array board using Hall-effect sensors is used to individually record the current passing through eight parallel connected cells in two different electrical configurations, showing highly heterogeneous current distribution. Characteristic “waves” of current and temperature are found to propagate along the parallel battery string and cell rebalancing is found to occur over hundreds of seconds with individual cell currents of up to 1 C rate.

1. Introduction

Parallel battery strings are used in most battery packs to meet the high capacity and power requirements of applications such as automotive traction.^[1] For example, the Tesla Model S 85 kWh battery pack consists of 74 cells (18650) connected in parallel, and six of these in series to form a single module. Sixteen of these modules combine to create a full battery pack. Battery management systems (BMSs) typically treat each parallel string as a single electrical unit in terms of the current and voltage measured,^[2] thus creating a knowledge gap in the resolution and fidelity of whole-pack monitoring. Understanding what is occurring at the individual cell level provides a means of improving the performance, longevity, and safety of battery packs.

The way in which individual cells in parallel connected multi-cell modules charge and discharge is a complex function of the battery type and chemistry, energy capacity, applied source/load, interconnection resistance, relative cell internal impedance, temperature distribution, cooling mechanism, and relative location of the individual cells within the parallel configuration.^[3–8] These factors, as well as manufacturing tolerances, which can be up to 25% for impedance^[9,10] and 9% for capacity,^[10,11] can lead to charge imbalance. This has important implications for pack state of health (SoH) and safety as charge imbalance can result in different degradation rates.^[12] Temperature gradients also have an impact on charge imbalance. As a cell heats up, its internal resistance decreases, resulting in increased current flow, further adding to the temperature imbalance.^[13,14] This scenario has the possibility to lead to thermal runaway if there are no safety mechanisms in place.

Rebalancing currents are internal module currents that rebalance the terminal voltage of parallel connected cells and can flow during charge/discharge, as well as after disconnection from the load/source. This can lead to charge flow that is unaccounted for by the BMS and may be beyond the rated current of individual cells. This can also result in temperature increase in the pack after the load has been disconnected, the nature of which is difficult to predict.^[15] These rebalancing currents should ideally be measured on a cell-by-cell basis, to inform the BMS so that safety and performance can be improved.


Figure 1 shows how rebalancing of cells connected in parallel can occur. After a charge/discharge, the state-of-charge (SOC) levels can be imbalanced due to the mechanisms described

R. Luca, Dr. M. Whiteley, T. Neville, Dr. T. Tranter, Dr. J. Weaving,
Prof. P. R. Shearing, Prof. D. J. L. Brett
Electrochemical Innovation Lab
Department of Chemical Engineering
University College London
WC1E 7JE, UK
E-mail: d.brett@ucl.ac.uk

Dr. M. Whiteley, Prof. P. R. Shearing, Prof. D. J. L. Brett
Advanced Propulsion Lab
UCL East
University College London
London E15 2JE, UK

Dr. T. Tranter, Prof. P. R. Shearing, Prof. D. J. L. Brett
The Faraday Institution
Quad One, Becquerel Avenue, Harwell Campus, Didcot OX11 0RA, UK

Prof. J. Marco
Warwick Manufacturing Group Department
The University of Warwick
Coventry CV4 7AL, UK

 The ORCID identification number(s) for the author(s) of this article can be found under <https://doi.org/10.1002/ente.202001014>.

© 2021 The Authors. Energy Technology published by Wiley-VCH GmbH. This is an open access article under the terms of the Creative Commons Attribution License, which permits use, distribution and reproduction in any medium, provided the original work is properly cited.

DOI: 10.1002/ente.202001014

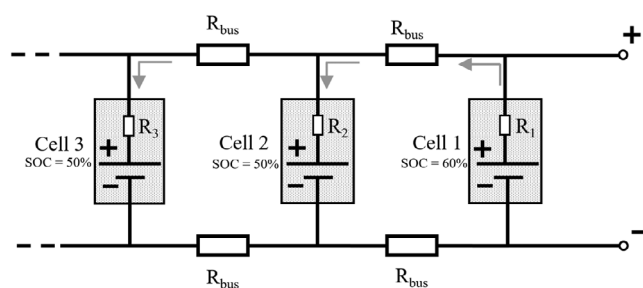


Figure 1. Parallel string of cells with different SOC levels. Example of cell rebalancing after charge. Cell 1 has a higher SOC due to the higher charge transferred from the lower resistive pathway to load. This results in rebalancing currents flowing from cell 1 into other cells in the parallel string.

earlier. This results in the local potential of cell 1 being higher than that of cell 2 and 3, which drives the rebalancing current.

Various experimental and modeling approaches have been adopted to improve the understanding of charge imbalance. Wu et al.^[15] used a Newman pseudo-2D (P2D)-based model with finite connection resistances to explore how charge imbalances are generated in parallel connected modules. The model was coupled with a lumped thermal model. They found that increasing the number of parallel cells increased the charge imbalance, with the cells closest to the load experiencing the highest currents. They also found that increasing the interconnect-to-battery impedance leads to a logarithmic increase in charge nonuniformity. Cycling around a narrow SOC range and pulse discharge resulted in the largest current imbalance. Rebalancing currents were also noted to cause further heating, which has the potential to lead to thermal runaway.

Hofmann et al.^[16] used a state-space model with linear open-circuit voltage (OCV) to solely investigate the effects of production parameter variations on current asymmetry. They then added a nonlinear OCV and found that this is the dominant cause of the effect.

Fill et al.^[17] present an analytical model for current distribution, SOC, and OCV differences in parallel battery strings. Monte Carlo simulations were used to correlate these differences with cell configuration, resistance, and capacity. They found a near-logarithmic relation between maximum current nonuniformity and the number of cells in parallel.

Bruen and Marco^[12] modeled and experimentally investigated current imbalance in parallel connected cells. They presented an ECM framework that can be expanded to incorporate any number of cells connected in parallel. The model was validated using four 3 A h 18650 cells. They measured the current of each cell using a high-precision, 10 mΩ, low-thermal-coefficient shunt resistor, which they confirmed is not the same as the absolute current passing through each cell when operating without shunt resistors due to the added resistance. They postulated that the use of a Hall-effect sensor would remove this disadvantage of added resistance, but the accuracy and resolution were too low for measuring rebalancing effects. To simulate the effect of cells with different internal resistances (SoH), each cell in a four-cell parallel string was aged a different amount (0, 50, 100, and 150 cycles). This created greater heterogeneity in cell current, with aged cells taking lower currents at the start of the discharge due to greater internal resistance.

Liu et al.^[18] studied the effects of cell-to-cell variations in parallel strings on performance and degradation using an experimentally verified single particle model. Their test case was six 5 A h Kokam lithium polymer pouch cells. They introduced a resistance of 10 mΩ between each parallel branch and a 1 mΩ (±5%) interconnect resistance used to measure the current into each cell. They showed that cells closest to the current collection points experience the highest currents and that placing cells with higher internal resistance in these locations can help to equalize cell-to-cell current distribution. They also report that placing the same high-internal-resistance cell in the location farthest from the current collection can result in an ≈6% reduction in accessible energy at 1.5 C.

Brand et al.^[19] investigated the current imbalance within pairs of parallel connected cells experimentally and theoretically with a simplified equivalent circuit model (ECM). They performed analysis on two case studies: pairs with different internal resistance but near-identical capacities (ΔR), and pairs with near-identical internal resistances but different capacities (ΔC). They used LEM LTSR 6 Hall-effect current transducers to measure individual cell currents. In the ΔR case, they found that initial currents were imbalanced before equalizing with continued constant current (CC). They also found current imbalances for the ΔC case, with currents dividing in proportion according to their capacities for long-lasting currents. However, their measurement technique required five sensors in total, two large-format Hall-effect sensors for cell currents up to ±19.2 A, two CTSR 0.6 P fluxgate current transducers for a higher precision measure of cell currents, which had a range of ±0.85 A, and a single differential fluxgate transducer to measure the difference between the cells. Their Hall-effect sensors had a current resolution of 42 mA and the fluxgate transducers had a current resolution of 13 mA. The complexity, cost, and size of this measurement setup clearly cannot be translated into a vehicle battery pack for on-board diagnostics in real-world applications. They also do not explain how the effects observed might propagate with the number of parallel connected cells higher than two.

Pastor-Fernandez et al.^[10] studied four parallel cells while cycling them to their end-of-life (EoL) condition. They measured cell current using a 10 mΩ shunt resistor and quantified their internal resistances using galvanostatic electrochemical impedance spectroscopy (EIS). They initially degraded each cell to a different amount by cycling it before testing. The initial SoH (capacity) difference was 40%, which converged to 10% by cycle 500. For an initial SoH (resistance) difference of 45%, the convergence was smaller, finishing at 30%. They found a linear relation between SoH (resistance) and cycle number that can be accounted for by a BMS.

Klein and Park^[6] performed a comprehensive investigation of five parallel connected 18650 cells containing different cathode chemistries: LiFePO₄/C₆ (LEF) and LiNiMnCoO₂/C₆ (NMC). Pulse and full capacity discharges at various SOC, C-rates, average temperatures, and levels of temperature nonuniformity were performed. Under charge-depleting conditions, the NMC group experienced greater current uniformity, and nearly uniform current distribution in the presence of nonuniform temperature. This study again used 10 mΩ shunt resistors to measure the cell currents. Their module was designed with bifurcating current pathways to ensure bus bar resistances were the same to each cell, which is typically not how modules are designed.

An et al.^[20] also used Hall-effect sensors to measure cylindrical cell currents. They used large-format sensors and placed two cells each within the hollow core of an FDIB C16-5P4O5 Hall-effect sensor. Each sensor had a current range of ± 5 A and a resolution of 20 mA. However, due to the large size of the Hall sensors used their method does not allow the study of tightly packed parallel connected cells similar to that found in automotive applications. Placing the Hall sensors around the outside of each cell may also lead to interference from internal cell currents—an effect that has not been quantified or discussed.

Hall-effect sensors offer the potential of nonintrusive measurement of cell current without introducing resistance into the module, as well as providing true bidirectional current measurement of charging, discharging, and current relaxation (rebalancing) when at open circuit. Modern manufacturing methods and the scale of the electronics industry have reduced the cost of Hall-effect sensors, so they now have the potential to be integrated as an on-board diagnostic tool in a BMS. By contrast, shunt resistors add resistance and an increased number of electrical connections to each cell, which could distort the current distribution.^[12] Shunt resistors also have a temperature dependence, which could further distort results. With high cell current, these errors will be amplified and parasitic power loss will become significant.

By understanding the distribution of current in parallel-connected battery systems, this study aims to contribute to previous research efforts by demonstrating a new, noninvasive current-measuring technique that has the scope to be implemented into vehicle battery systems as an on-board monitoring and diagnosis technique, and thereby help to improve BMS algorithms, aid battery designers with cell configuration and interconnection methods, help to optimize the bus bar specification, and examine the effect on module-level degradation and provide experimental data for model validation.

2. Experimental Section

2.1. Module Specification, Configuration, and Cycling

Figure 2 shows the custom-made battery module with an integrated Hall-effect sensor array placed just above the module casing and below the bus bar. The cells used were commercial

Samsung 20R 18650s with NMC cathodes, graphite anodes, and 2000 mA h capacity. The centre-to-centre spacing of each cell was 20.2 mm, leaving an air gap of 1.8 mm between each cell. The module was cycled at ambient temperature with passive cooling. In “common-end” configuration, cell 1 is closest to both positive and negative current collectors, and in “opposite-end” configuration cell 8 is closest to the positive current collector and cell 1 is closest to the negative (Figure 3).

Figure 2b shows a close-up of the Hall-effect sensor positioning. The pick-up wire, shown coming out of plane, can be seen in the centre of the ferrite core with the concentric magnetic field lines shown in perforated red. This design allows the Hall-effect sensors to be integrated in close proximity to the cell electrode terminal, and even form part of the module casing.

The negative bus bar was created by spot welding two parallel 0.15 mm thick nickel strips (Cambridge Energy Solutions Ltd, UK) to the negative terminals of the cells. Nickel is a commonly used material in small battery modules for bus bars; in this case it introduced an interconnection resistance of 1.42 m Ω between each cell. For the positive terminals, a pick-up wire was soldered to a small piece of nickel strip that was spot welded to the positive tabs of each cell. The pick-up wire was then fed through the ferrite core. The positive bus bar was the same as that for the negative, with each pick-up wire attached using crocodile clips. The pick-up wires were pure copper with 24 core stands, each with a gauge of 0.25 and 35 mm in length. Each pick-up wire and crocodile clip assembly introduced 2.93 ± 0.30 m Ω contact resistance between the cell and the bus bar. However, this is less than a shunt resistor and as each pick-up is effectively in series with the cell it should not change the overall characteristics of the current distribution. This design also allows for integration into typical module manufacturing methods that use fuse wire between the cell and bus bar, in which case it would not increase the cell connection resistance. The module was cycled using a Gamry Reference 3000 with 30 A booster.

2.2. Hall-Effect Sensor Operation and the Multisensor Array Board

A Hall-effect sensor measures the current through a wire by detecting the induced magnetic field, its output voltage being

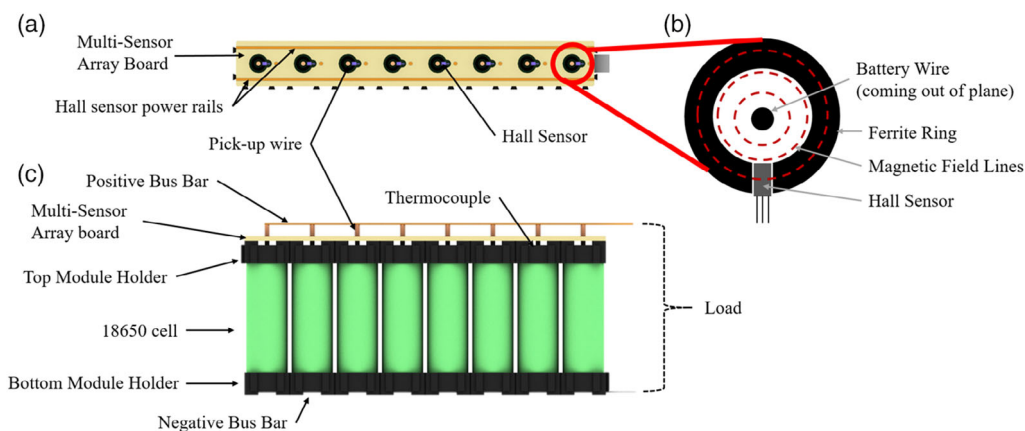


Figure 2. a) Top view of the MSAB, b) close-up of the Hall sensor and ferrite core, and c) side profile of the eight-cell linear module.

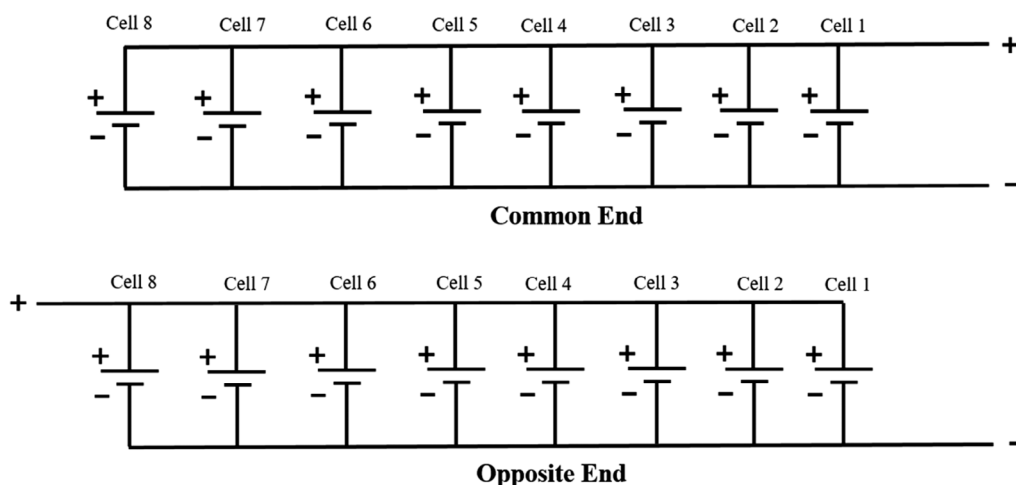


Figure 3. Electrical configuration of the module.

directly proportional to the magnetic field strength. Its working principle is based on the Hall effect and Ampere’s law, which states that the magnetic field from a straight wire is proportional to the current passing through it^[21] (Equation (1)), where μ_0 is the permeability of free space, μ_r is the relative permeability of the ferrite core, I is current, B is the magnetic flux density, and r is the radial distance from the wire to the Hall-effect sensor.

$$B = \frac{\mu_0 \mu_r I}{2\pi r} \quad (1)$$

The multi-sensor array board (MSAB) provides a power supply to all eight Hall-effect sensors, voltage measurement output, and structural support for the sensors. The Hall-effect devices used were Honeywell SS490A1 Series miniature ratiometric sensors, with a cost of £1.90 per unit. However, modern Hall-effect sensors can cost as little as 10p when bought at scale; therefore, implementing the MSAB onto a representative battery module on the vehicle will have little effect on total pack cost. It should be noted that there will be an extra cost per cell associated with the voltage measurement for each Hall sensor. The total thickness of the MSAB was 4 mm, which is also an acceptable space requirement. Each sensor takes a 5 V power supply across its ground and positive pins and its output voltage (between ground and sense pin) at zero magnetic flux is half its input voltage. The sensors are bidirectional, so they can measure a discharging current indicated by a voltage below 2.5 V, as well as charging current. The Hall-effect sensor was placed within the circumference of a small ferrite core with relative permeability (μ_r) of 10 000 to collect and increase the magnetic flux density, increasing the signal-to-noise ratio. This measurement technique resulted in a current resolution of 20 mA.

Thermocouples were used to give point measurements on the body of the cell. Type-T thermocouples were placed two-thirds up the body of each cell and affixed using polyimide tape. The data from the Hall-effect sensors, thermocouples, and cell voltages were sampled at 100 Hz using a National Instruments CompactRIO Chassis with 9022 and 9024 voltage and temperature modules, respectively. This was fed into a custom NI LabVIEW program to convert each voltage into current using calibration data. The MSAB was calibrated by passing a range of small

currents (0.2 to -0.2 A) through each cell before fixing it to the positive bus bar. The transfer function $y = mx + c$ was fitted to each data set for calibration. The average resulting R^2 value was 0.9998. There was a small drift in the Hall sensor output of 75 mA throughout the duration of each test. By subtracting the total measured current (Hall measured current) from the known total current (Gamry current) at each time step the total drift of the module can be calculated, which can then be removed from each cell, assuming the drift was equal for each cell. This assumption is justified as Hall drift is driven by two main factors: time and temperature. As each sensor was operated for the same amount of time, this should be equal, and the temperature change seen from the thermal imaging was approximately the same for each sensor as well.

2.3. Thermal Imaging of Module

A thermal imaging camera (X6903sc, FLIR Systems France, Croissy-Beaubourg, France) was used to measure the temperature distribution during operation and current rebalancing. A 25 mm, $f/2.5$ lens was used and the system was calibrated within the range 10–90 °C. Data were recorded at 1 Hz using commercially available software (FLIR Research IR, FLIR Systems, France). The thermal camera provided the temperature profile of the whole module, including the pick-ups, bus bar, and distribution along the cell surfaces.

3. Results

3.1. Charge and Discharge Profiles

The module was charged and discharged in two different electrical configurations, shown in Figure 3. It was charged with a CC of 16 A, equivalent to 1 C per cell, to a bus voltage of 4.2 V. It was then taken to open circuit and left to reach thermal equilibrium with the environment. A discharge current of 16 A was then imposed until the module reached 2.5 V, where it was again taken to open circuit.

Figure 4 shows the current experienced by each cell in the module, with Figure 4a,b for “common-end” configuration

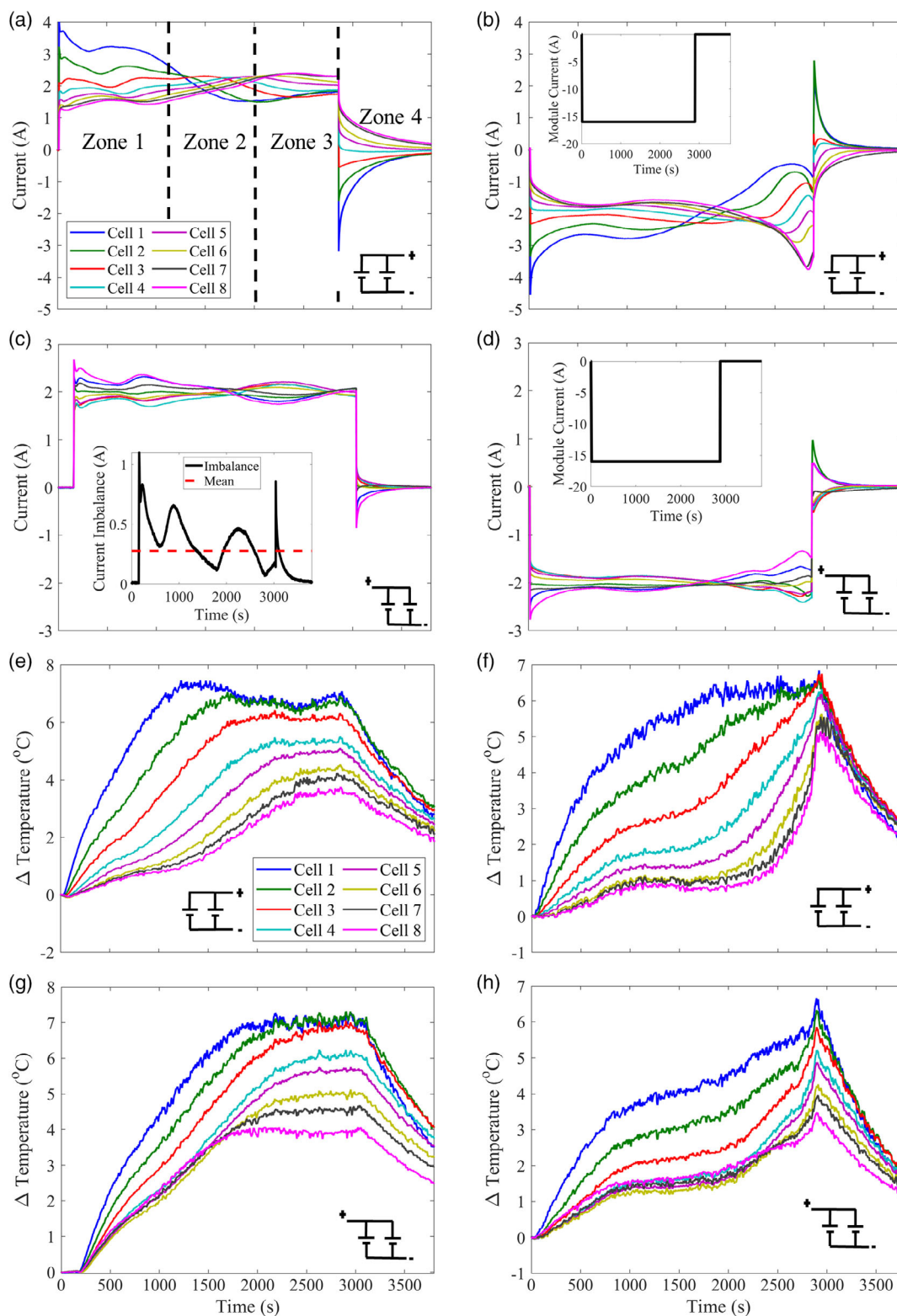


Figure 4. Charge and discharge current of a,b) common-end configuration and c,d) opposite-end configuration, respectively. The electric circuit in the bottom right corner represents the electrical configuration. The insets in (b) and (d) show the summation of Hall-effect sensor currents and the inset in (c) shows the current imbalance (maximum cell current minus minimum cell current) for that charge. e,f) Single point temperature measurements of common-end charge and discharge and g,h) opposite-end charge and discharge, respectively. The legend in (a) applies to all plots.

charge and discharge and Figure 4c,d for “opposite-end” charge and discharge, respectively.

It can be seen that in each case there is a complex current response from each cell composed of plateaus and “waves” that traverse along the module. However, to simplify interpretation, each charge/discharge/OCV process can be notionally separated into four zones of operation: the first (zone 1), where the current is dominated by cells from a particular location/s of the parallel string; zone 2, a crossover period; zone 3 where the trend is reversed and the current is dominated by the complimentary set of cells to that in zone 1; and zone 4, where the module is put into OCV mode and rebalancing currents occur.

Considering the common-end charging configuration (Figure 4a), the cell closest to the charging source initially experiences the highest current at over 4 A, with cells further from the terminal experiencing lesser current, down to ≈ 1.2 A for cell 8. For cell 1, this is equivalent to a 2 C charging rate, and remains above the rated charging rate of 2 A for 1400 s. Cells 3 and 4 have the most “balanced” and constant charging current across the range. The crossover zone 2 occurs between ≈ 1200 and 2000 s with the cell 1 current decreasing to below the current of cell 8 at 1520 s. In zone 3, cell 8 takes the largest share of current and cell 1 the least.

When the module was taken to OCV in zone 4, cells 1, 2, and 3 began discharging into the other cells (shown as a negative current) to rebalance the module. Cell 1 experienced a peak rebalancing current of 3.5 A, significantly higher than the intended charging current of 2 A during this test. During extreme fast charging, such a current could cause the cell to exceed the maximum current safety limit. Yet here it is experienced as an internal module current under notional OCV conditions.

Figure 4b shows the individual cell currents during common-end discharge. Again, in zone 1, cell 1 took the largest share of current, peaking at 4.8 A, and remained above 2 A for nearly 2000 s. Peak current imbalance occurred when the load was initially applied, which is a phenomenon-experienced throughout all the tests conducted. The zone 2 crossover period occurs between ≈ 1500 and 2500 s before cell currents begins to diverge, with cell 8 again taking the largest share of current at the end of charge. Rebalancing again occurs when the module is taken to OCV, with peak currents experienced by cell 2 and lasting ≈ 1000 s.

The characteristic “waves” and “plateaus” are likely to be caused by each cell’s internal resistance being a function of the SOC and the shape of the OCV–SOC curve. The effect temperature has on internal resistance is smaller but not insignificant. The temperature profile of the module is characterized in Section 3.3. Dynamic internal resistance measurements and modeling are needed to fully understand this phenomena.

Figure 4c,d shows the cell-by-cell current results for opposite-end operation. For this electrical configuration, the cells closest to the current collectors at either end of the parallel string (cells 1 and 8) experienced the highest currents (2.32 and 2.68 A, respectively), with cells in the middle of the module experiencing the least when the charging source was initially applied. This general trend is supported by modeling studies.^[15] Again, there is a minimum that occurs within zone 1 where the cells begin to converge prior to the crossover that occurs in zone 2. This

phenomena is particularly clear during charging periods. The more symmetric current collection of the opposite-end configuration results in a much more homogeneous distribution of current, with a mean current imbalance of 0.28 and 0.29 A for charge and discharge, respectively, compared to 1.02 and 0.93 A for common-end operation. Current imbalance was simply defined by the difference between the maximum and minimum cell current. The symmetric nature of the opposite-end current collection configuration results in a symmetric “butterfly profile” in zones 1 and 3, with a narrow crossover in zone 2 at ≈ 1750 s.

Figure 4e–h shows the point temperature measurements of each cell during charge and discharge for each electrical configuration. In the common-end configuration, the cells closest to the current collection experienced the greatest temperature change due to Ohmic heating from the initial high current magnitude in zone 1. However, in the opposite-end configuration the cells’ thermal response did not follow the current response, with cells heating in the same order as the common-end configuration. This counterintuitive result is explained with the use of thermal imaging in Section 3.3.

A differential voltage measurement was taken across each cell during the charge and discharge profiles. The results of this can be seen in Figure 5. The cells closest to the current collection were found to have the highest voltages in both electrical configurations. The voltage follows the cell current distribution observed in Figure 4. During common-end configuration charge (Figure 5a), cell 1 charged to a voltage of 4.15 V and cell 8 to a voltage of 3.98 V, which is a disparity of 0.17 V. A voltage measurement by the charging system next to cell 8 would pose a risk of overcharging certain cells within the module. Conversely, recording the voltage next to cell 1 results in undercharging the farthest cells, reducing the utilization of the whole module, as shown in Figure 5e. Upon going to OCV, all voltages collapsed, reaching a common voltage after ≈ 1000 s. The small voltage differences between each cell drive significant rebalancing currents, as shown in Figure 4a.

The opposite-end configuration vastly reduced the voltage disparity between the cells, with only 0.04 V between cell 8 and cell 4, therefore the much smaller rebalancing current.

Integration of current measurements shows the total charge transferred of each cell (Figure 5e–h). The absolute current was integrated to show the total charge passed through each cell, not the final resting charge. Again, the common-end configuration resulted in much larger disparity between each cell, a difference of 21.5% between cell 1 and cell 8. In opposite-end configuration, there was a much smaller charge disparity of 7.8% between cell 8 and cell 4. However, over the lifetime of the module, this charge inequality in the opposite-end configuration still poses a high risk of heterogeneous degradation of the cells. During the module CC charging phase, in common-end configuration the module took on a total of 12.63 A h compared to 12.80 A h in opposite-end configuration, a reduction in capacity of 1.3%. Although many manufacturers still opt for the common-end configuration due to practicality, it is stressed that the opposite-end configuration is a superior electrical configuration due to increased capacity, potentially reduced module degradation, and increased safety.

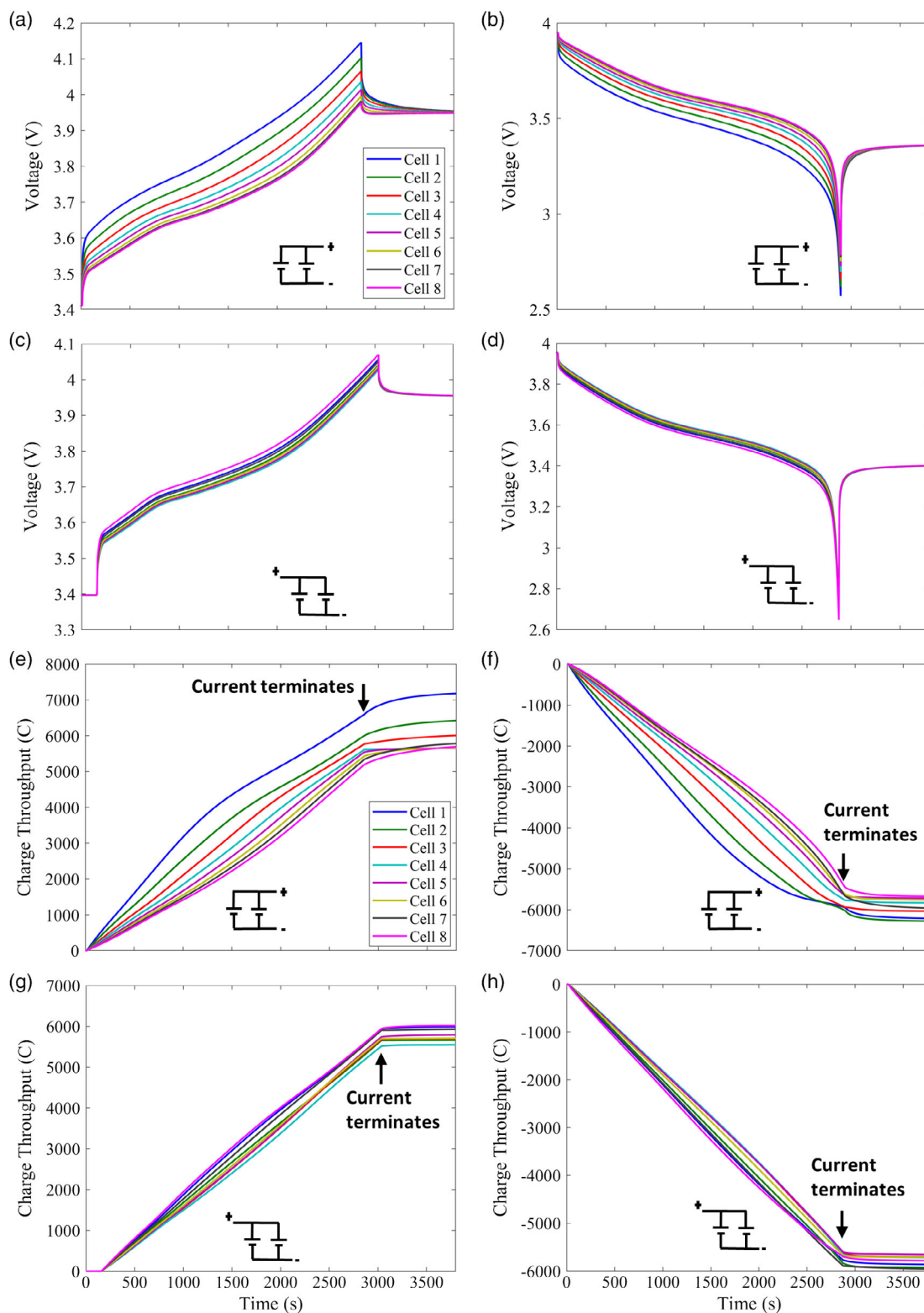


Figure 5. Voltage response of all cells during a,b) common-end operation and c,d) opposite-end operation. Cumulative charge for each cell during e) common-end charge, f) common-end discharge, g) opposite-end charge, and h) opposite-end discharge. The magnitude of the charge was used during the charge summation; therefore, the negative sign represents module discharge in (f) and (h).

3.2. Current Imbalance under Pulse Discharge

The module was pulsed with discharge current according to the protocol in Table 1. This profile was chosen to explore the current distribution under changing loads representative of periods in an automotive drive cycle, such as acceleration.

This was done to quantify the ratio of current imbalance at different module currents. This quantity is defined to be χ

$$\chi = \frac{I_{\text{cell,max}} - I_{\text{cell,min}}}{I_{\text{total}}}$$

Table 1. Pulse current protocol.

Step	Operation	Current [A]	Duration [s]
1	Discharge	5	15
2	Rest	–	15
3	Discharge	10	15
4	Rest	–	15
5	Discharge	15	15
6	Rest	–	15
7	Discharge	20	15
8	Rest	–	15
9	Discharge	25	15
10	Rest	–	60

where $I_{\text{cell,max}}$ is the maximum current experienced by any cell, $I_{\text{cell,min}}$ is the minimum current experienced by any cell, and I_{total} is the total module current. The leading edge of the pulses was used to calculate this quantity as this is where the maximum current imbalance occurs.

Figure 6a shows the current measurements for the common-end configuration pulse test. Again, cell 1 took the highest share of current, and cell 8 the least. For the 25 A pulse, cell 1 peaked at 7 A when the nominal average current per cell should have been 3.125 A. Only 15 s at this high current was enough to cause a rebalancing current of nearly 1 A. Opposite-end operation again reduced the magnitude of current imbalance; however, this was still 2 A at the 25 A current pulse. These tests again show cells 1 and 8 taking on the highest current, with cells 4 and 5 experiencing the least. These tests show that more consideration is needed when designing battery modules as cells closest to the current collection will undergo higher stresses, increasing the long-term degradation of the battery pack.

The pulse sequence was started at 35% SOC, and the subsequent pulses in the common-end configuration resulted in a 2% SOC change, equivalent to 0.313 A h removed from the module. The cells' internal resistance as a function of SOC can be seen in Figure 6d. This was obtained using galvanostatic EIS with the real resistance at 1 Hz taken for the plot. The change in module SOC caused an average internal resistance change of 0.23%, which should not significantly affect the distribution observed.

Figure 6c shows the calculated χ for each current pulse and electrical configuration. During common-end operation, the ratio of current imbalance did not significantly depend on the total

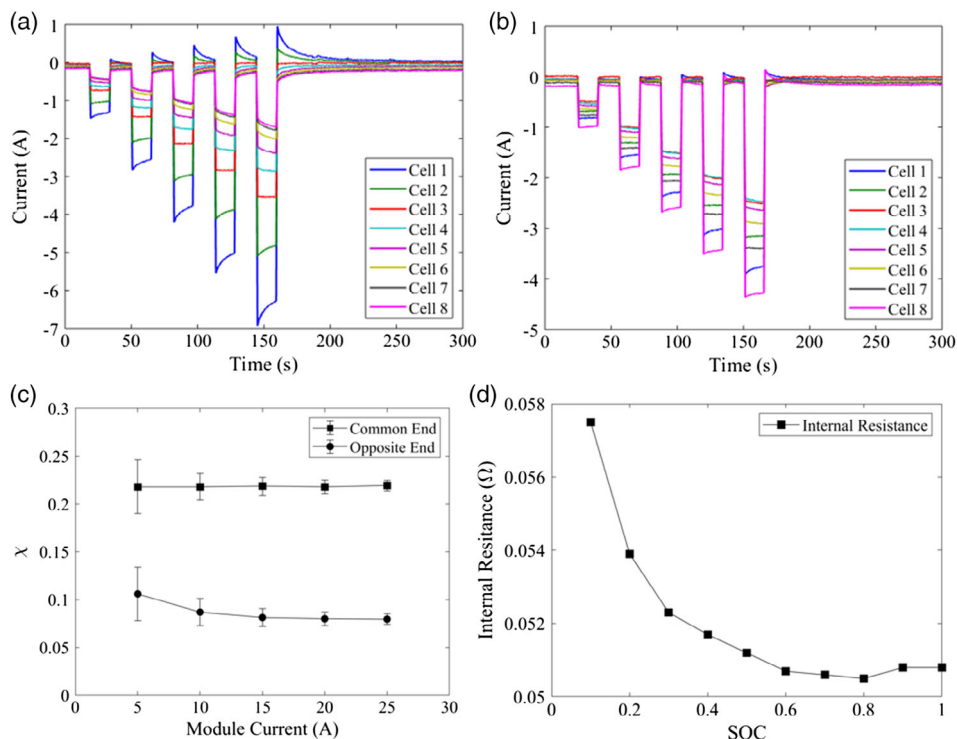


Figure 6. Cell currents of module in a) “common-end” configuration and b) “opposite-end” configuration. c) Ratio of current imbalance (χ) for different module currents and d) cell internal resistance at different SOCs. The internal resistance was obtained using galvanostatic EIS with the real resistance at 1 Hz taken for the plot.

module current. During opposite-end operation, χ was flat at high currents but increased slightly at low module currents. The overall ratio of imbalance significantly decreased from the common-end to the opposite-end operation. This implies that the ratio of current imbalance is largely dependent on pack design and not total module current.

3.3. Whole-Cell and Module Dynamic Temperature Profiling Using Thermal Imaging

The battery module was thermally imaged during the charge and discharge profiles of both electrical configurations to provide the temperature distribution over the whole cell/module surface. The results are shown in **Figure 7**. Thermal imaging of individual 18650 cylindrical cells has previously shown that the heat generation is concentrated at individual cell terminals,^[22] and this is observed here at the individual-cell level. The thermal gradient across the eight cells caused by the current imbalance can be clearly seen in both charge and discharge in both electrical configurations. The temperature of the pick-up wires is a particularly clear indicator of the current passing through each cell and

corresponds to the current measured using the Hall-effect sensors.

Figure 7 shows a single frame of each recording taken at 2500 s. An image subtraction using the first frame of each recording was used to reduce emissivity variation issues and calculate change in temperature. The temperature profiles closely match that of the single-point temperature measurement in Figure 4. Cell 8 experienced little heat generation despite having the highest share of current in the opposite-end configuration. The current can be clearly seen in the pick-up wire above cell 8. It is expected that the high current passing through the nickel bus bar under cell 1 significantly influenced the temperature distribution throughout the module, with the heat transferring longitudinally up each cell. The significant heat generation in the negative module lead in Figure 7d and the fact that cells 1, 2, and 3 are hot while the pick-up wires remain cool is evidence for this conclusion. Passive cooling to the environment also resulted in striking heat generation in the cell-to-cell spacing. This is quantified in the profile plots below each thermal image with the double-ended arrow in Figure 7a showing the line where the profiles were taken. For the common-end charging condition

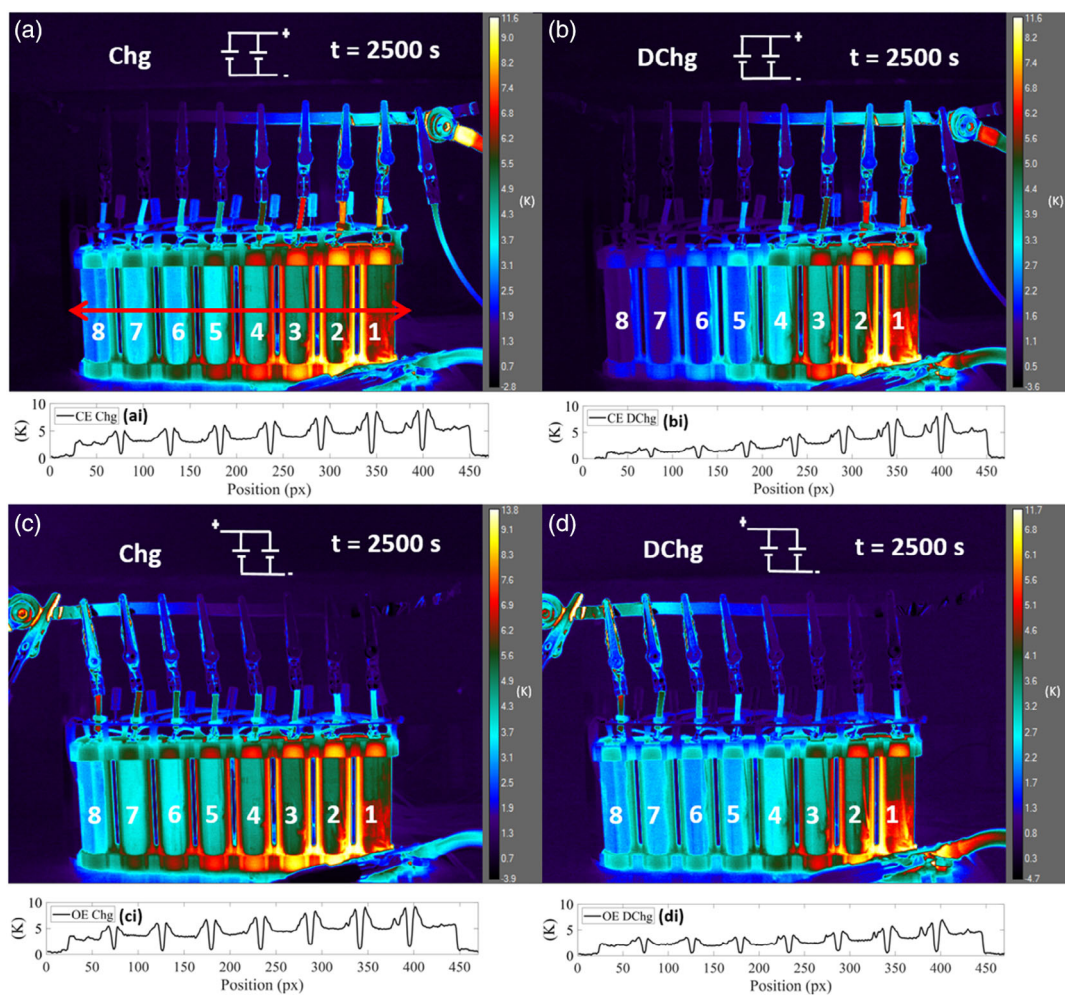


Figure 7. Thermal images of the whole module at 2500 s during a) common-end charge, b) common-end discharge, c) opposite-end charge, and d) opposite-end discharge. The numerical values in temperature scale represent temperature change.

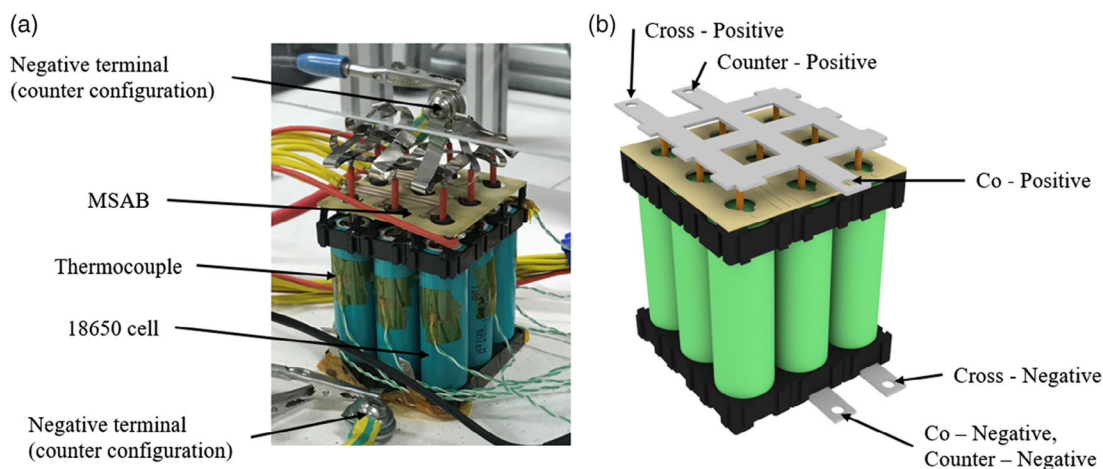


Figure 8. a) Image of the cell cluster and b) diagram showing different load electrical configurations.

at 2500 s, it can be determined from the profile that cell 7 had an average temperature difference of 2.06 °C between the open cell body and the intercell spacing. Cell 2 at the hotter end of the module experienced a temperature difference of 3.93 °C, a significant thermal gradient which is likely to be exacerbated by conventional pack cooling techniques as these often only cool a single side of the cell, missing the intercell spacing.

3.4. Expansion to Larger Modules

As a demonstration, the MSAB was applied to a cluster of nine cells in a 3 × 3 layout, as shown in **Figure 8**. This was done to 1) demonstrate the technique could be applied to modules of any size and orientation and 2) investigate the effect of the load electrical configuration on the current balance in tightly packed cells. The module was constructed using the same techniques as that described in Section 2.1.

The module was charged and discharged also at 1 C per cell, resulting in 18 A this time due to having nine cells. Figure S1, Supporting Information, shows the distribution of current amongst the cells when the load was initially applied and just before going to OCV. Generally, the cells follow the same conclusions as before and in Wu et al.,^[15] where cells closest to current collection experience the largest current initially, which is inverted at some point during the charge/discharge. Plots of each cell current and temperature during cycling can be found in Figure S2–S4, Supporting Information.

4. Conclusion

Parallel connected cells experience vast current heterogeneities, with cells close to current collection experiencing more than twice their intended current. It is clear that BMSs need to take this more into consideration as cell rebalancing currents can exceed 1 C and last several minutes, which jeopardizes cell and module safety and lifetime through well-established degradation processes. Cell-by-cell current measurements revealed a total charge difference of 21.5% in common-end configuration,

which could potentially result in heterogeneous cell degradation. Our data support modeling studies that show an inversion in cell currents closest/farthest to current collection; however, our results show more complex profiles with characteristic plateaus and waves during charge and discharge. The micro-Hall-effect sensor array presented is a significant development from previous studies using Hall-effect sensors, dramatically reducing the setup size, paving the way for on-board current sensing while maintaining a high current accuracy of 20 mA. The approach also allows the internal resistance of each parallel cell to be determined in future via module-wide hybrid pulse power characterization or EIS measurements. Module-level thermal imaging revealed intracell thermal gradients of nearly 4 °C as a result of reduced cooling in the intercell spacing. The approach also allows for on-board diagnostics and improved BMSs, which could deliver increased pack lifetimes by understanding cell-by-cell degradation within a module. From this, a long-term cycling study is suggested to see how different cells age within the parallel string. New BMS algorithms or improvements in design are needed to maximize the performance and lifetime of battery packs. Such improvements could be a minimization of bus resistance or implementation of cell capacitors to remove high peak rebalancing currents.

Supporting Information

Supporting Information is available from the Wiley Online Library or from the author.

Acknowledgements

R.L. acknowledges a studentship from the EPSRC Centre for Doctoral Training in Fuel Cells and their Fuels (EP/L015749/1). The Electrochemical Innovation Lab (EIL) is supported through EPSRC projects (EP/M014371/1, EP/S018204/2, EP/R023581/1, EP/P009050/1, EP/L015749/1, EP/M009394/1, EP/M023508/1). P.R.S. acknowledges funding from the Royal Academy of Engineering (CIET1718/59). T.T., P.R.S., and D.J.L.B. acknowledge the Faraday Institution (EP/S003053/1).

Conflict of Interest

The authors declare no conflict of interest.

Data Availability Statement

Research data are not shared.

Keywords

automotive batteries, battery management systems, cell rebalancing, current imbalance, Hall-effect sensors, lithium-ion cells, parallel cells

Received: November 23, 2020

Revised: January 11, 2021

Published online:

-
- [1] X. A. M. C. Zhang, *Vehicle Power Management*, Springer, London **2011**, p. 259.
- [2] C. Bonfiglio, W. Roessler, in *2009 IEEE Vehicle Power and Propulsion Conf.*, IEEE, Dearborn, MI, USA **2009**, pp. 304–309, <https://doi.org/10.1109/VPPC.2009.5289837>.
- [3] K. Rumpf, A. Rheinfeld, M. Schindler, J. Keil, T. Schua, A. Jossen, *J. Electrochem. Soc.* **2018**, *165*, A2587.
- [4] F. Chang, F. Roemer, M. Baumann, M. Lienkamp, *World Electric Vehicle J.* **2018**, *9*, 1.
- [5] Y. Zhang, J. Zheng, S. Lin, F. Bai, W. H. Tanveer, S. Cha, X. Wu, W. Feng, *Int. J. Energy Res.* **2018**, *42*, 2835.
- [6] M. P. Klein, J. W. Park, *J. Electrochem. Soc.* **2017**, *164*, A1893.
- [7] N. Yang, X. Zhang, B. Shang, G. Li, *J. Power Sources* **2016**, *306*, 733.
- [8] A. Fill, S. Koch, A. Pott, K. P. Birke, *J. Power Sources* **2018**, *407*, 147.
- [9] R. Gogoana, M. B. Pinson, M. Z. Bazant, S. E. Sarma, *J. Power Sources* **2014**, *252*, 8.
- [10] C. Pastor-Fernández, T. Bruen, W. D. Widanage, M. A. Gama-Valdez, J. Marco, *J. Power Sources* **2016**, *329*, 574.
- [11] B. Kenney, K. Darcovich, D. D. MacNeil I. J. Davidson, *J. Power Sources* **2012**, *213*, 391.
- [12] T. Bruen, J. Marco, *J. Power Sources* **2016**, *310*, 91.
- [13] L. Chen, Z. Lü, W. Lin, J. Li, H. Pan, *Measurement* **2018**, *116*, 586.
- [14] T. Huria, M. Ceraolo, J. Gazzarri, R. Jackey, *Mech. Eng. Therm* **2012**, *1*.
- [15] B. Wu, V. Yufit, M. Marinescu, G. J. Offer, R. F. Martinez-Botas, N. P. Brandon, *J. Power Sources* **2013**, *243*, 544.
- [16] M. H. Hofmann, K. Czyrka, M. J. Brand, M. Steinhardt, A. Noel, F. B. Spingler, A. Jossen, *J. Energy Storage* **2018**, *20*, 120.
- [17] A. Fill, S. Koch, K. P. Birke, *J. Energy Storage* **2019**, *23*, 37.
- [18] X. Liu, W. Ai, M. Naylor Marlow, Y. Patel, B. Wu, *Appl. Energy* **2019**, *248*, 489.
- [19] M. J. Brand, M. H. Hofmann, M. Steinhardt, S. F. Schuster, A. Jossen, *J. Power Sources* **2016**, *334*, 202.
- [20] F. An, J. Huang, C. Wang, Z. Li, J. Zhang, S. Wang, P. Li, *J. Energy Storage* **2016**, *6*, 195.
- [21] D. Griffiths, *Introduction to Electrodynamics*, Pearson **2005**.
- [22] J. B. Robinson, J. A. Darr, D. S. Eastwood, G. Hinds, P. D. Lee, P. R. Shearing, O. O. Taiwo, D. J. Brett, *J. Power Sources* **2014**, *252*, 51.